Optics Letters

Silicon carbide double-microdisk resonator

Xiyuan Lu,[1,4,5] Jonathan Y. Lee,[2] Steven D. Rogers,[1] and Qiang Lin[2,3,*]

[1]Department of Physics and Astronomy, University of Rochester, Rochester, New York 14627, USA
[2]Department of Electrical and Computer Engineering, University of Rochester, Rochester, New York 14627, USA
[3]Institute of Optics, University of Rochester, Rochester, New York 14627, USA
[4]Current affiliation: Maryland Nanocenter, University of Maryland, College Park, Maryland 20742, USA
[5]e-mail: xnl9@umd.edu
*Corresponding author: qiang.lin@rochester.edu

Received 9 July 2019; accepted 31 July 2019; posted 5 August 2019 (Doc. ID 372196); published 23 August 2019

We demonstrate the first silicon carbide (SiC) double-microdisk resonator (DMR). The device has a compact footprint with a radius of 24 μm and operates in the ITU high frequency range (3–30 MHz). We develop a multi-layer nanofabrication recipe that yields high optical quality ($Q \sim 10^5$) for the SiC DMR. Because of its strong optomechanical interaction, we observe the thermal-Brownian motions of mechanical modes in a SiC DMR directly at room temperature for the first time, to the best of our knowledge. The observed mechanical modes include fundamental/second-order common modes and fundamental differential (D1) modes. The D1 modes have high mechanical qualities >3800 at around 18.4 MHz tested in vacuum. We further show that optomechanical interactions, including linear and nonlinear optomechanical spring effects, can be observed in a SiC DMR at sub-milliwatt optical power. The SiC DMR has great potential for low-power optomechanical sensing applications in harsh environments.

https://doi.org/10.1364/OL.44.004295

Silicon carbide (SiC) has been extensively studied in micro-electro-mechanical systems (MEMS) sensors [1] and has shown unique advantages for harsh environments [2,3] and biocompatible applications [4] due to its exceptional mechanical properties and chemical inertness [5]. Recently, thanks to the developing nanofabrication technologies, SiC nanophotonics has attracted significant interest in the fields of cavity optomechanics, nonlinear optics, and quantum optics [6–22]. Cavity optomechanics allows efficient interactions between optical and mechancial modes in a micro-/nano-meter scale [23] and can further improve the performance over current MEMS sensors. For this purpose, various optomechanical structures have been studied in SiC, including photonic crystals (nanobeam [13], zipper [17], etc.) and microdisk resonators [19,20]. However, the optical properties of these optomechanical devices are still restricted by current nanofabrication technologies, in particular, thin film growth and dry etching. As a result, the efficiencies of current optomechanical devices are yet to be improved. In previous SiC microdisk work [19], although high mechanical f-Q product has been demonstrated, the optomechanical interaction is not strong enough, and the thermal-Brownian motion of the mechanical modes cannot be observed directly at room temperature. Therefore, a modulated optical pump is needed to drive the mechanical mode in order to characterize the device.

To this end, one optomechanical structure of interest is the double-microdisk resonator (DMR) [24–29]. The DMR has useful properties of mutli-mode optical/mechanical mode operation and strong optomechanical coupling, and has versatile applications, including wavelength routing [24], coherent mechanical excitation/cooling [25,27], photonic control [26], and mechanical synchronizing [28]. We note that a DMR is different from a single microdisk in that the optomechanical coupling rate (g_{OM}) depends on the vertical dimension (i.e., gap), and not the radial dimension (i.e., radius). Because the DMR typically has a gap ≈150 nm, its g_{OM} is much larger than the value from single microdisk, which makes the DMR particularly suitable for direct observation of the thermal-Brownian motion of the mechanical modes. However, a SiC DMR has not been demonstrated yet, although various SiC nanophotonic devices, including microdisk and photonic crystals have been developed [13,17,19,20]. In contrast, the DMR has been studied in silicon oxide (SiO_2) [24,25,27,30] and silicon nitride (Si_3N_4) [26,28,29] extensively. The major challenge for the SiC DMR is on nanofabrication and, particularly, on etching multilayer photonic structures smoothly.

The SiC DMR has advantages over SiO_2 and Si_3N_4 DMRs on several aspects. First, SiC has a much larger refractive index (≈2.6) than SiO_2 (≈1.5) and Si_3N_4 (≈2.0). As a result, the SiC DMR can have a better mode confinement, a smaller effective mass, and a smaller device footprint, when compared to SiO_2 and Si_3N_4 DMRs. Secondly, SiC is one of the hardest materials in nature (only second to diamond) and is robust against mechanical resistance and shock waves [2,3]. Moreover, unlike SiO_2 or Si_3N_4, SiC has chemical stability over most corrosives [5]. These properties make SiC suitable for sensing and other applications in extreme environments [1–3].

In this Letter, we introduce a fabrication recipe for SiC multi-layer processing and, for the first time, to the best of our knowledge, demonstrate a SiC DMR. The fabrication recipe uses aluminum oxide (Al_2O_3) as a hard mask and Si as a

sacrificial layer, which can readily be applied to other multilayer material platforms. The fabricated device exhibits high optical qualities, high mechanical qualities, and efficient optomechanical interactions. The mechanical modes can be observed directly through thermal-Brownian motion, without resorting to the optical pump-probe scheme [19]. The optical spring effect is observed with <100 μW power. Moreover, a nonlinear optical spring effect, that is, light-induced quadratic spring softening, is observed for sub-milliwatt optical power. Our SiC optomechanical device has great potential in sensing and metrology applications under harsh environments.

The device has two functioning layers of SiC microdisks separated by a silica layer, sitting on a silicon pedestal, as shown in Figs. 1(a) and 1(b). The total thickness of the multilayer is 1 μm. Both SiC layers are 400 nm thick, and the sandwich oxide layer is 200 nm thick. The DMR has an outer radius of 24 μm. The silica undercut is 3.5 μm, and the silicon undercut is between 8 and 10 μm, depending on the substrate orientation. The mechanical mode under study is the fundamental differential mode indicated by solid lines in Fig. 1(a). The device supports bonding/anti-bonding modes, where electric fields have the same/contrary phases in the top and bottom microdisks, correspondingly [Fig. 1(c)]. The bonding/anti-bonding modes, as the names suggest, exert attractive/repelling optical force on the two SiC layers, respectively. The optical force is given by $F = -n_{\mathrm{cav}}\hbar g_{\mathrm{OM}}$, where F is the optical force (positive, repelling; negative, attracting), n_{cav} is the intracavity photon number which scales with input optical power, $\hbar$ is the reduced Planck constant, and g_{OM} is the optomechanical coupling strength. The optical force drives mechanical motion which, in turn, modifies the resonance frequencies [Fig. 1(d)]. The amplitude of such optomechanical coupling is described by g_{OM}. Figure 1(e) shows the dependence of g_{OM} on the separated air gap.

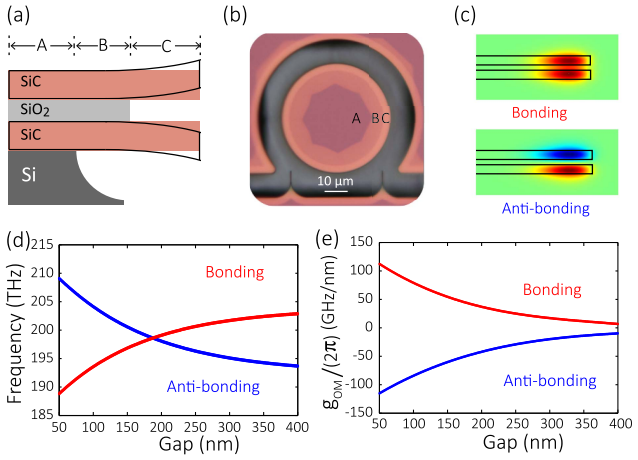

Fig. 1. (a) Schematic view of a cross section of the device, with solid lines indicating the mechanical motion of the fundamental differential (D1) mode. Notations A, B, and C (top) indicate different regions of the device, i.e., the Si pedestal area, SiC/SiO_2/SiC area, and SiC/air/SiC area, respectively. (b) Microscopic image of a SiC DMR. Regions A, B, and C show different colors under microscope. (c) Cross-sectional view of two types of optical mode profiles, i.e., the fundamental bonding and anti-bonding modes, where darkness and color indicate the amplitude and phase of the dominant electric field, respectively. Both modes are transverse electrically polarized. (The dominant electric field is in the radial direction.) (d) Cavity resonance frequencies and (e) their optomechanical coupling rates between the D1 mechanical mode and the displayed optical modes.

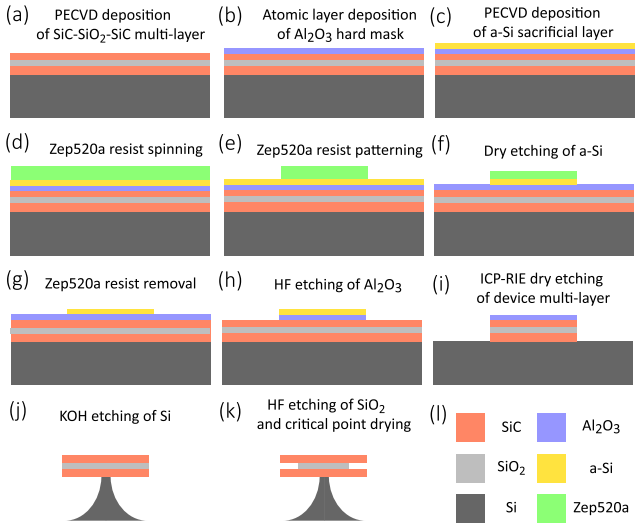

Fig. 2. (a)–(k) Process flow of the fabrication of a SiC DMR with Al_2O_3 as a hard mask. PECVD, plasma-enhanced chemical vapor deposition; ICP-RIE, ion-coupled plasma reactive-ion etching. (l) Colors are used to label different materials.

We have developed a nanofabrication recipe for such a multi-layer SiC device. The process flow is shown in Fig. 2. Three device layers SiC/SiO_2/SiC are subsequently deposited onto the silicon substrate by plasma-enhanced chemical vapor deposition (PECVD). An Al_2O_3 layer of 80 nm is deposited onto the device layers by atomic layer deposition as the hard mask for dry etching of the device layers. A 30 nm a-Si layer is deposited on top of the Al_2O_3 layer as a hard mask for wet etching of the Al_2O_3 layer. An electron beam resist, Zep520a, is then spun onto the silicon layer. The resist is patterned by electron beam lithography. The pattern is transferred to silicon by reactive-ion etching using CF_4/SF_6 gases. After removal of Zep520a, the Al_2O_3 mask is etched by HF acid. The device layer is then etched by inductively coupled plasma reactive-ion etching (ICP-RIE) using CF_4/O_2 gases. The Al_2O_3 is removed by a hydrofluoric (HF) acid dip. The device is then undercut by heated potassium hydroxide (KOH). Since the etching rates of silicon by KOH depend on the crystalline orientation, the silicon undercut has an octagon shape [Fig. 1(b)]. Finally, the gap SiO_2 layer is partially removed by HF acid followed by critical point drying to avoid the adhering of two SiC layers.

One critical aspect of this nanofabrication recipe is the use of Al_2O_3 as a hard mask. The etching selectivity of SiC to Al_2O_3 is 15:1. This selectivity is much larger than those of SiC to SiO_2, Zep520a, and maN under the same etching recipe, which are 1:2, 1:10, and 1:5, respectively. As a result, only 60 nm Al_2O_3 is needed to etch the 1 μm device layer (containing 800 nm SiC and 200 nm SiO_2). Although Al_2O_3 is a good mask for dry etching, it can be easily removed through wet etching by either acid or base, which gives unique flexibility in fabrication process. However, one issue with the wet etching, in particular, HF acid, is the surfactant effect. HF acids tend to attack the interface of Zep520a/Al_2O_3 and lift off the Zep520a. Therefore,

we use an extra Si sacrificial layer as a solution, because the Si/Al_2O_3 boundary is free of such a surfactant effect. Although this recipe contains quite a few steps, all the fabrication steps utilize conventional nanofabrication technologies and can be easily applied by general users to other materials/devices.

We characterize the optical and mechanical modes of the fabricated device by analyzing the transmitted light in optical and RF frequencies, respectively. The cavity transmission in Fig. 3(a) shows many high Q optical modes with reasonable coupling. For example, the resonance mode at 1535 nm is critically coupled and has an intrinsic Q of 1.0×10^5, as shown in Fig. 3(b). The thermal-Brownian motions of the mechanical modes in such systems, due to the high optical Q and optomechanical coupling [Fig. 1(e)], can be measured directly by the continuous-wave lasers through optomechanical transduction, as shown in Figs. 3(c) and 3(d). In atmosphere, the mechanical mode of the DMR has a low mechanical quality of 12 at a frequency of 19.7 MHz, which is mainly due to the squeeze-film damping from the air between two SiC disks. In vacuum, the mechanical quality boosts over 100 times (up to >3800), as shown in Fig. 3(d), and the frequency is shifted to 18.4 MHz. The mechanical Q is insensitive to the pressure changes at the operated vacuum level. Besides the main peak, two more side peaks are resolved at 18.7 and 19.4 MHz with similar mechanical qualities. These modes have different frequencies because the octagon Si pillar [Fig. 1(b)] from KOH wet etching [Fig. 2(j)] breaks the rotational symmetry and lifts the degeneracy of the mechanical modes.

The simultaneous resonant enhancement of light and mechanical motion leads to intensive optomechanical interaction. As a result, we only need <100 μW to observe optical spring effects in the SiC DMR. In a side-band unresolved regime, the mechanical frequency shift ($\delta\Omega_m$) is given by [23]

$$\delta\Omega_m(\Delta) = \frac{n_{\mathrm{cav}}\Delta}{(\Gamma_t/2)^2 + \Delta^2}\frac{\hbar g_{\mathrm{OM}}^2}{m_{\mathrm{eff}}\Omega_{\mathrm{m}}}. \quad (1)$$

Here n_{cav}, $\hbar$, and g_{OM} represent the intracavity photon number, reduced Planck constant, and optomechanical coupling strength, respectively. Δ is the laser-cavity detuning, and a positive/negative Δ represents a blue-/red-detuning laser. Γ_t represents a loaded cavity linewidth, which is given by ω_o/Q_t, where ω_o is the optical frequency, and Q_t is the loaded cavity quality factor. m_{eff} is the effective mass. Ω_m is the natural mechanical frequency. This equation shows two characteristics of an optical spring. First, the spring softening/hardening, that is, the decrease/increase in the mechanical frequency, scales with the intracavity photon number and, hence, the input power. Secondly, the mechanical spring is softened when the laser is red-detuned ($\Delta < 0$) and hardened when blue-detuned ($\Delta > 0$).

Optical tuning of the mechanical spring, the optical spring effect, is a direct result of the optomechanical coupling [23], which has found broad applications in sensing and signal processing [27,31,32]. The observation of the optical spring effect is a signature of strong optomechanical coupling in the device. To observe such an effect, we use a mode at 1537 nm with an loaded optical quality of $Q_t = 5.8 \times 10^4$. Figures 4(a) and 4(b) show the optical spring effects at 10 and 100 μW optical powers, respectively. The optical mode is undercoupled with a minimum transmissivity of 60%. A comparison of these two figures validates the dependence of the optical power for the optical spring effect, i.e., the stronger the optical power is dropped into the cavity, the larger the mechanical spring frequency is increased. Here we only observe spring hardening because the opto-thermal bistability prevents us from locking the laser at the red-detuning side. To go to the blue-detuning side, we use an optical mode at 1522 nm with an optical quality $Q_t = 2.8 \times 10^4$. Because this value is smaller than the previous case, the cavity mode has a smaller opto-thermal effect (at the same input power). Therefore, such a mode allows us to observe both spring softening (bottom) and hardening (top), as shown in Fig. 4(c).

Besides the linear optical spring effect, SiC DMR also supports the quadratic spring effect; that is, the optical spring has a quadratic dependence on the laser-cavity detuning. We tune a laser to an optical mode with $Q_t = 1.1 \times 10^4$. In this case, quadratic spring softening is observed, where both red detuning and blue detuning soften the mechanical spring, as shown in Fig. 4(d). This light-induced spring softening effect is similar to electostatic spring softening in the MEMS device [33]. In particular, the bonding mode has attractive force that has a negative quadratic dependence on relative displacement (δx), closely resembling that of a electrostatic capacitance, which corresponds to a softening of the spring.

In summary, we have demonstrated, to the best of our knowledge, the first SiC DMR. The high optical and mechanical qualities enable us to observe thermal-Brownian motion of mechanical modes directly at room temperature for the first time, to the best of our knowledge. The efficient optomechanical coupling also allows us to observe linear and nonlinear mechanical spring effects with sub-miliwatt optical power. SiC DMRs have the potential to boost the performance of current sensing technology and to provide versatile

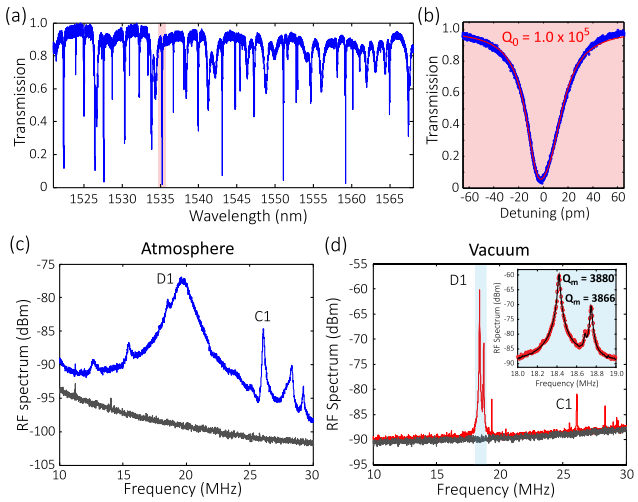

Fig. 3. (a) Cavity transmission of the SiC DMR. (b) Cavity mode at 1537 nm is critically coupled and has an intrinsic optical quality of 1.0×10^5. (c) and (d) Optomechanically transduced RF spectra tested in the atmosphere and vacuum show fundamental differential (D1) and common (C1) modes. The inset of (d) shows the fitting of D1 modes in black. In the D1 mode, the top and bottom microdisks oscillate with contrary phases, as illustrated in Fig. 1(a). In the C1 mode, both top and bottom microdisks oscillate in phase.

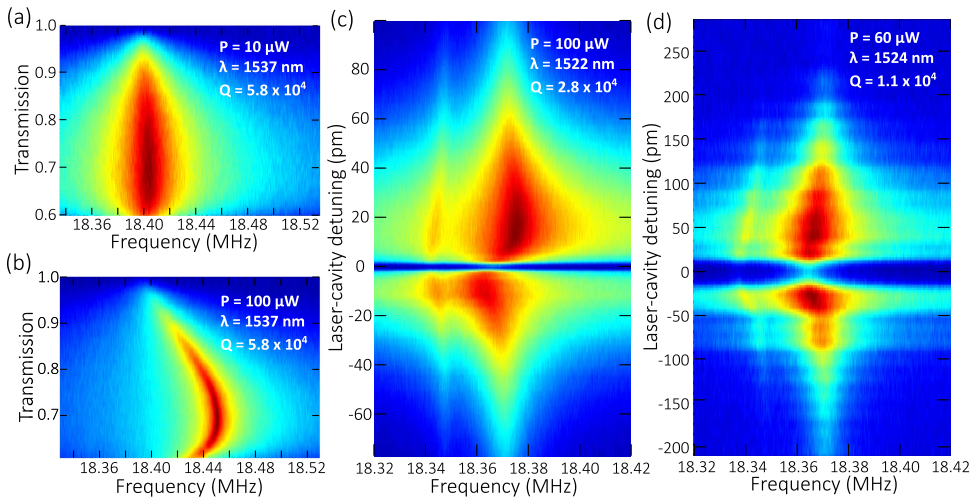

Fig. 4. (a) and (b) Power dependence of the linear optical spring effect. The intracavity power is adjusted by laser-cavity detuning. The detuning controls the cavity transmission (T), and the intracavity power is given by P(1-T), where P represents the input power. (c) Asymmetric dependence of laser-cavity detuning can be observed for the linear optomechanical spring. When the laser is red detuned to the cavity (positive laser-cavity detuning), the mechanical frequency is higher than the natural frequency (18.37 MHz). When the laser is blue detuned to the cavity (negative laser-cavity detuning), the mechanical frequency is lower than the natural frequency. (d) Symmetric dependence of laser-cavity detuning for the quadratic spring effect. Unlike the linear spring effect, for both red and blue detuned cases, the mechanical frequency is lower than the natural frequency.

functionality, particularly in harsh environments and biology applications.

Funding. National Science Foundation (NSF) (ECCS-1610674, ECCS-1408517, ECCS-1509749, EFMA-1641099, NNCI-1542081); National Institutes of Health (R21EB0249988).

Acknowledgment. The fabrication was performed in part at the Cornell NanoScale Science and Technology Facility (CNF), a member of the National Nanotechnology Coordinated Infrastructure (NNCI), which is supported by the National Science Foundation.

REFERENCES

1. M. Mehregany, C. A. Zorman, N. Rajan, and C. H. Wu, Proc. IEEE **86**, 1594 (1998).
2. M. Mehregany and C. A. Zorman, Thin Solid Films **355–356**, 518 (1999).
3. D. G. Senesky, B. Jamshidi, K. B. Cheng, and A. P. Pisano, IEEE Sens. J. **9**, 1472 (2009).
4. S. E. Saddow, *Silicon Carbide Biotechnology*, 2nd ed. (Elsevier, 2016).
5. G. L. Harris, *Properties of Silicon Carbide* (INSPEC, 1995).
6. B.-S. Song, S. Yamada, T. Asano, and S. Noda, Opt. Express **19**, 11084 (2011).
7. S. Yamada, B.-S. Song, J. Upham, T. Asano, Y. Tanaka, and S. Noda, Opt. Express **20**, 14789 (2012).
8. J. Cardenas, M. Zhang, C. T. Phare, S. Y. Shah, C. B. Poitras, B. Guha, and M. Lipson, Opt. Express **21**, 16882 (2013).
9. M. Radulaski, T. M. Babinec, S. Buckley, A. Rundquist, J. Provine, K. Alassaad, G. Ferro, and J. Vučković, Opt. Express **21**, 32623 (2013).
10. X. Lu, J. Y. Lee, P. X.-L. Feng, and Q. Lin, Opt. Lett. **38**, 1304 (2013).
11. A. P. Magyar, D. Bracher, J. C. Lee, I. Aharonovich, and E. L. Hu, Appl. Phys. Lett. **104**, 051109 (2014).
12. G. Calusine, A. Politi, and D. D. Awschalom, Appl. Phys. Lett. **105**, 011123 (2014).
13. J. Y. Lee, X. Lu, P. X.-L. Feng, and Q. Lin, in *2014 Conference on Lasers and Electro-Optics (CLEO)* (Optical Society of America, 2014), paper SF1M.2.
14. S. Yamada, B.-S. Song, S. Jeon, J. Upham, Y. Tanaka, T. Asano, and S. Noda, Opt. Lett. **39**, 1768 (2014).
15. X. Lu, J. Y. Lee, P. X. Feng, and Q. Lin, Appl. Phys. Lett. **104**, 181103 (2014).
16. X. Lu, J. Y. Lee, S. Rogers, and Q. Lin, Opt. Express **22**, 30826 (2014).
17. J. Y. Lee, X. Lu, and Q. Lin, Appl. Phys. Lett. **106**, 041106 (2015).
18. M. Radulaski, T. M. Babinec, K. Müller, K. G. Lagoudakis, J. L. Zhang, S. Buckley, Y. A. Kelaita, K. Alassaad, G. Ferro, and J. Vučković, ACS Photonics **2**, 14 (2015).
19. X. Lu, J. Y. Lee, and Q. Lin, Sci. Rep. **5**, 17005 (2015).
20. J. Lee, H. Zamani, S. Rajgopal, C. A. Zorman, and P. X.-L. Feng, J. Micromech. Microeng. **27**, 74001 (2017).
21. F. Martini and A. Politi, Appl. Phys. Lett. **112**, 251110 (2018).
22. T. Fan, H. Moradinejad, X. Wu, A. A. Eftekhar, and A. Adibi, Opt. Express **26**, 25814 (2018).
23. M. Aspelmeyer, T. J. Kippenberg, and F. Marquardt, Rev. Mod. Phys. **86**, 1391 (2014).
24. J. Rosenberg, Q. Lin, and O. Painter, Nat. Photonics **3**, 478 (2009).
25. Q. Lin, J. Rosenberg, X. Jiang, K. J. Vahala, and O. Painter, Phys. Rev. Lett. **103**, 103601 (2009).
26. G. S. Wiederhecker, L. Chen, A. Gondarenko, and M. Lipson, Nature **462**, 633 (2009).
27. Q. Lin, J. Rosenberg, D. Chang, R. Camacho, M. Eichenfield, K. J. Vahala, and O. Painter, Nat. Photonics **4**, 236 (2010).
28. M. Zhang, G. S. Wiederhecker, S. Manipatruni, A. Barnard, P. McEuen, and M. Lipson, Phys. Rev. Lett. **109**, 233906 (2012).
29. M. Zhang, G. Luiz, S. Shah, G. Wiederhecker, and M. Lipson, Appl. Phys. Lett. **105**, 051904 (2014).
30. C. Bekker, C. G. Baker, R. Kalra, H.-H. Cheng, B.-B. Li, V. Prakash, and W. P. Bowen, Opt. Express **26**, 33649 (2018).
31. A. G. Krause, M. Winger, T. D. Blasius, Q. Lin, and O. Painter, Nat. Photonics **6**, 768 (2012).
32. W. Yu, W. C. Jiang, Q. Lin, and T. Lu, Nat. Commun. **7**, 12311 (2016).
33. H. Droogendijk, C. Bruinink, R. G. P. Sanders, A. M. Dagamseh, R. J. Wiegerink, and G. J. M. Krijnen, J. Micromech. Microeng. **22**, 065026 (2012).